

MnAs nanoclusters embedded in GaAs studied by x-ray diffuse and coherent scattering

M. Moreno, B. Jenichen, V. Kaganer, W. Braun, A. Trampert, L. Däweritz, and K. H. Ploog

Paul-Drude Institute of Solid-State Electronics, Hausvogteiplatz 5-7, 10117 Berlin, Germany

(Received 27 February 2003; published 26 June 2003)

The structure of phase-separated (Ga, Mn)As, annealed at high temperature ($\sim 700^\circ\text{C}$), is studied by x-ray diffraction techniques. Analysis of the x-ray diffuse and coherent scattering reveals two types of clusters: (1) small clusters detected by diffuse scattering through the distortions they produce in the host matrix and (2) larger clusters with MnAs structure giving rise to coherent diffraction peaks. The average sizes for the two cluster types are estimated to be 5 and 18 nm, respectively. The smaller clusters are found to be of vacancy type. Their density is estimated to be $1.8 \times 10^{16} \text{ cm}^{-3}$. The hexagonal lattice of the larger MnAs crystallites is found to be compressed along the $[\bar{2}110]$ direction by -0.49% with respect to the bulk hexagonal MnAs lattice. The host zinc blende matrix is found to be under a -0.20% tensile strain.

DOI: 10.1103/PhysRevB.67.235206

PACS number(s): 75.50.Pp, 81.07.-b, 61.10.-i, 75.50.Tt

I. INTRODUCTION

Today much effort is being devoted to the synthesis and study of hybrid ferromagnet-semiconductor heterostructures because of the interesting physical phenomena involved and the relevance of integrating magnetism into optoelectronic device technology.¹⁻⁸ The synthesis of ferromagnetic nanosized particles embedded in a semiconductor host is of particular interest.^{9,10} Such materials offer great flexibility for exploring carrier spin scattering, because the carrier densities in semiconductors are tunable over a wide range and their spatial confinement can be controlled. Despite the great potential for spin-electronic (spintronic) devices, properties of ferromagnetic dots in semiconductors have been scarcely investigated.

MnAs nanoclusters embedded in GaAs—hereafter denoted GaAs:MnAs—can be obtained by annealing molecular beam epitaxy (MBE)-grown (Ga, Mn)As alloys.¹¹⁻¹⁷ The GaAs:MnAs granular material has a ferromagnetic-superparamagnetic behavior (depending on the cluster size) at room temperature^{12,17,18} and exhibits giant magnetoresistance and giant magneto-optical effects.^{13,14,19-21} It shows a high degree of crystalline perfection,¹⁶⁻¹⁸ and excellent compatibility with III-V heterostructures.¹⁵ All these properties make the GaAs:MnAs granular material very well suited for application in magneto-optoelectronic devices.^{22,23}

The use of the electron spin, in future spintronic devices, requires structures with well-controlled material properties. Besides the control of the magnetic properties, there are strict requirements for structural perfection in these devices. In this paper, we report results of structural studies of phase-separated (Ga, Mn)As by x-ray diffuse and coherent scatterings. Our motivation is to provide a nondestructive nanoscale structural characterization of the material.

II. EXPERIMENTAL DETAILS

The sample fabrication process included two steps: MBE growth of the ternary (Ga, Mn)As alloy and subsequent thermal annealing. First, a GaAs buffer layer was grown at 600°C on a GaAs(001) substrate. The substrate was then

cooled down to 255°C for the growth of 100 nm of LT-GaAs (GaAs grown at low temperature) followed by ~ 550 nm of ternary (Ga, Mn)As. The (Ga, Mn)As growth rate was 5 nm/min and the As_4/Ga beam-equivalent-pressure ratio was ~ 20 . After growth, the sample was annealed *ex situ* in a rapid thermal annealing (RTA) oven under flowing nitrogen gas and covered with a GaAs wafer piece. In the RTA treatment, the sample was heated from 200°C to 700°C in 20 s, annealed at 700°C for 20 s, and cooled down to 400°C in 12 s. After the sample preparation, the structural properties were analyzed by high-resolution conventional and grazing-incidence x-ray diffraction measurements.

Grazing-incidence diffraction (GID) measurements were carried out shortly after the sample fabrication, after exposure to air, in a z -axis six-circle diffractometer²⁴ using synchrotron radiation from the U125/2 wiggler source at the synchrotron BESSY II (Berlin, Germany). A double-crystal monochromator allowed to chose the x-ray energy of 12 keV (wavelength $\lambda \approx 1.03 \text{ \AA}$). The GID measurements were carried out in vertical scattering geometry. Angular (ω) scans were obtained by rotating the sample about the horizontal surface normal. Radial ($\omega-2\theta$) scans were obtained by rotating the sample and the detector about the surface normal, the detector rotating twice as fast and in the same direction as the sample.

Conventional high-resolution x-ray diffraction (HRXRD) measurements were carried out in a double/triple-crystal diffractometer combining a 18-kW rotating-anode generator (Rigaku) and a Bede D3 high-precision goniometer. Two grooved dislocation-free high-purity Ge crystals in dispersive (+, +) setting were used as monochromator,^{25,26} producing an x-ray beam with 5% of the intrinsic width of the $\text{Cu } K_{\alpha 1}$ line ($\lambda = 1.54 \text{ \AA}$). The conventional diffraction measurements were carried out in the usual horizontal scattering geometry. Angular (ω) scans were obtained by rocking the sample about the vertical axis, parallel to the sample surface and orthogonal to the scattering plane. Radial ($\omega-2\theta$) scans were obtained by rotating the sample and the detector about the vertical axis, the detector rotating twice as fast and in the same direction as the sample.

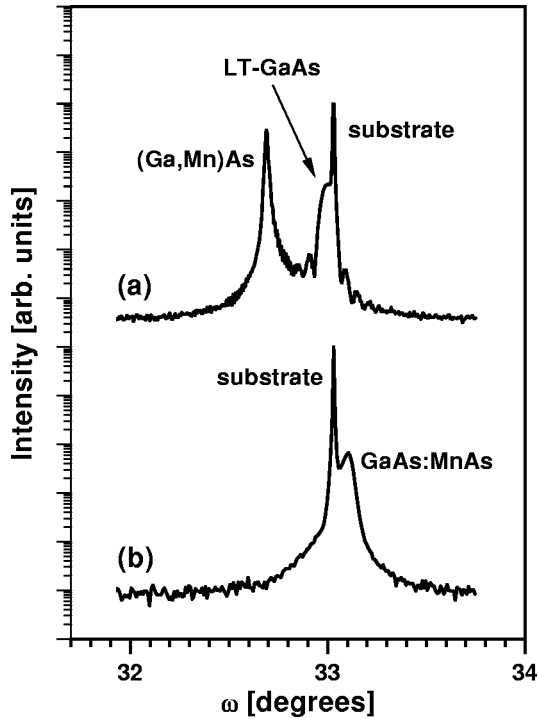


FIG. 1. High-resolution ω - 2θ XRD scans across the (004) symmetric Bragg reflections in a (Ga, Mn)As/LT-GaAs/GaAs(001) sample, recorded (a) before and (b) after annealing.

III. RESULTS

A. Coherent scattering

Conventional HRXRD was used to analyze the phase separation occurring upon annealing. Figure 1 shows ω - 2θ scans across the (004) symmetric reflection in the (Ga, Mn)As/LT-GaAs/GaAs(001) sample: (a) before and (b) after annealing. Before annealing, in addition to the GaAs substrate peak, two intense peaks are revealed corresponding to coherent diffraction in the LT-GaAs buried layer and in the (Ga, Mn)As top layer. From the HRXRD data, the Mn content in the (Ga, Mn)As layer is estimated to be 8.5% at most.²⁷ Upon annealing, the Mn atoms leave the zinc blende lattice to form clusters embedded in GaAs. The strain state of the (Ga, Mn)As layer changes from highly compressive [Fig. 1(a)] in the as-grown material, to slightly tensile [Fig. 1(b)] in the matrix of the granular material. The GaAs:MnAs matrix is determined to be compressed in the [001] direction by $(\Delta a/a)_{[001]} = -0.20\%$.

Transmission electron microscopy¹⁷ and selected-area electron diffraction²⁸ analysis of phase-separated (Ga, Mn)As material have shown that the granular layer may contain hexagonal MnAs clusters with a well-defined orientation with respect to the zinc blende GaAs matrix: the (0001) basal planes of the MnAs crystallites are parallel to $\{111\}$ GaAs planes, and the $\langle\bar{2}110\rangle$ MnAs directions are parallel to $\langle 110\rangle$ or $\langle 1\bar{1}0\rangle$ GaAs directions. There are four possible orientations for the MnAs crystallites, such that the (0001) MnAs planes are parallel to any of the four $\{111\}$ GaAs planes. In the sample investigated here, we did not succeed to detect the weak diffraction signal from MnAs

crystallites, using conventional x-ray diffraction, because of the relatively strong contribution of thermal diffuse scattering in this type of measurements. In order to improve the dynamic range, we carried out GID measurements, using synchrotron radiation. By using grazing incidence of the beam, the penetration of the x rays into the bulk crystal is limited. An optimum signal-to-noise ratio is obtained when the angle of incidence is equal to the critical angle for total external reflection.²⁹ Then the measurement is highly surface sensitive, and the contribution of thermal diffuse scattering from the bulk is dramatically reduced, which allows weak signals to show up.

We have succeeded to detect coherent diffraction from MnAs crystallites embedded in GaAs in a grazing-incidence/grazing-exit geometry, using synchrotron radiation. Figure 2 shows a ω - 2θ scan across the (220) reflection in the GaAs matrix of the granular layer. The incidence and exit angles were both set to 0.3° , which is close to the critical angle for total external reflection in GaAs. Three peaks are apparent in Fig. 2. The most intense peak corresponds to the (220) reflection in the matrix of the granular layer. Two weaker peaks are visible on either side of the main peak. They correspond to coherent diffraction in differently oriented MnAs crystallites. The weak peak at a larger angle corresponds to the $\{\bar{2}110\}$ reflections in MnAs crystallites whose (0001) basal planes are parallel either to $(\bar{1}\bar{1}1)$ or to $(1\bar{1}\bar{1})$ GaAs planes (see the right inset in Fig. 2). In these crystallites, the $\{\bar{2}110\}$ MnAs planes are exactly parallel to the (110) planes of the GaAs matrix. The weak peak at a smaller angle corresponds to the $\{0\bar{1}12\}$ reflections (not equivalent to the $\{\bar{2}110\}$ reflections) in MnAs crystallites whose (0001) basal planes are parallel either to (111) or to $(\bar{1}\bar{1}\bar{1})$ GaAs planes (see the left inset in Fig. 2). In these crystallites, the $\{0\bar{1}12\}$ MnAs planes are tilted by about 6° towards GaAs $(11\bar{1})$, with respect to the (110) planes of the GaAs matrix. Although the MnAs $\{0\bar{1}12\}$ reflection is not aligned with the GaAs (220) reflection, it is detected due to the elongated shape of the diffraction maxima in grazing-incidence measurements.²⁹ The detection of coherent diffraction from the MnAs crystallites in the GID measurements indicates that the oxidation of the sample surface was not severe, and the near surface region kept good structural quality.

From the position of the $(\bar{2}110)$ MnAs peak in Fig. 2, the interplanar distance in the MnAs crystallites along the $[\bar{2}110]$ direction was determined to be $a_{[\bar{2}110]}^{\text{cluster}} = 1.853 \text{ \AA}$. This is close to, but smaller than, the corresponding interplanar distance in bulk hexagonal MnAs $a_{[\bar{2}110]}^{\text{bulk}} = 1.862 \text{ \AA}$ (Ref. 30). Thus, the lattice of the MnAs crystallites is found to be compressed along the $[\bar{2}110]$ direction by $(\Delta a/a)_{[\bar{2}110]} = -0.49\%$.

We interpret the large width of the $(\bar{2}110)$ MnAs peak in Fig. 2 as a result of the small size of the crystallites. The Scherrer equation^{31,32}

$$L = \frac{0.94\lambda}{\Delta \cos \theta_B} \quad (1)$$

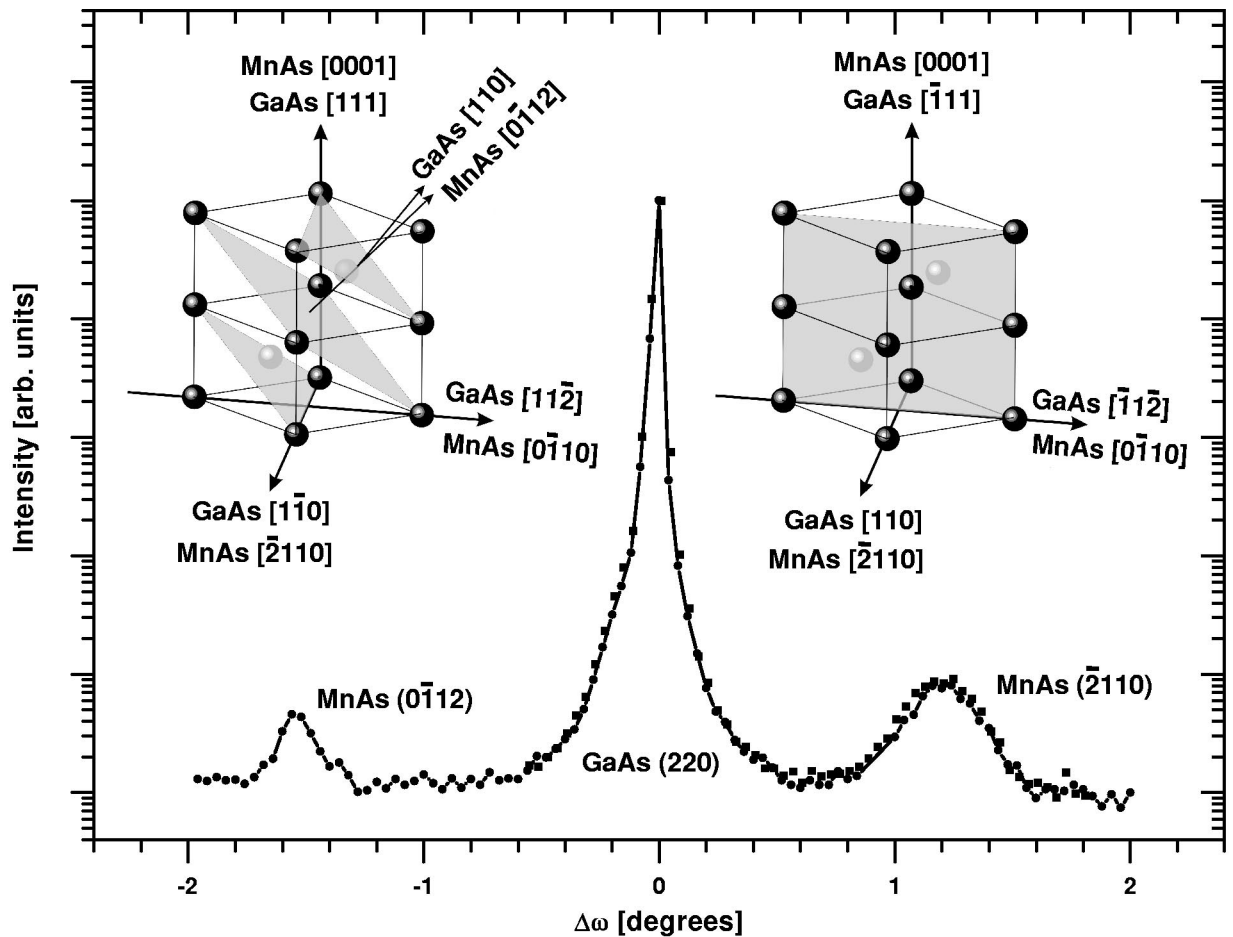


FIG. 2. ω - 2θ scans (grazing-incidence measurements) across the (220) reflection in the matrix of the GaAs:MnAs granular layer. Two independent measurements on the same sample are displayed (circles and squares). The solid line is a guide to the eye. The weak peaks correspond to the $(\bar{2}110)$ and $(0\bar{1}12)$ reflections in differently oriented MnAs crystallites, as illustrated in the respective insets that indicate the corresponding diffracting planes.

relates the crystallite size L to the peak broadening Δ in ω - 2θ scans. Here, λ is the x-ray wavelength, θ_B is the Bragg angle, and Δ is the full width at half maximum of the diffraction peak (in radians). Equation (1) gives the size of the crystallites in the direction perpendicular to the diffracting planes. Hence, the average size of the MnAs precipitates in the $[\bar{2}110]$ direction is estimated to be $L \approx 18$ nm.

B. Diffuse scattering

The analysis of diffuse scattering near Bragg reflections is a powerful method to study defect clusters that induce lattice distortions in crystalline materials.^{33–63} This technique has been used very successfully in studying point defects, dislocation loops, and precipitates in metals^{45–47} and semiconductors,^{48–63} including GaAs.^{59–63} We have recorded a map of the reciprocal space near the (004) reflection (Fig. 3) to study the symmetry of the diffuse scattering in the GaAs:MnAs layer. Our experimental setup for conventional HRXRD offered the possibility to use an analyzer crystal to record reciprocal space maps. However, in order to improve

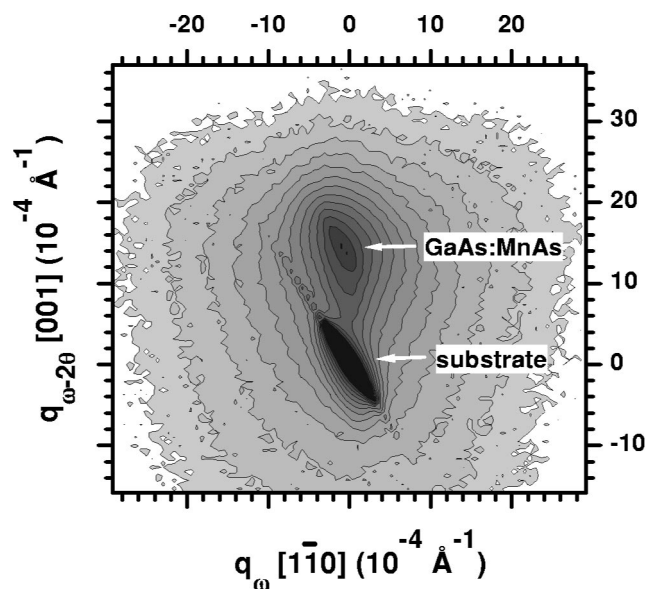


FIG. 3. Reciprocal space map near the (004) reflections in the annealed (granular) sample.

the experimental sensitivity and to keep the intensity of the diffuse scattering sufficiently high, we have used two aligned narrow slits (instead of the analyzer crystal) in front of the detector, and the x-ray beam was not collimated in the vertical direction orthogonal to the diffraction plane. The reciprocal-space map shows two intense peaks corresponding to coherent diffraction in the GaAs substrate and in the GaAs:MnAs matrix as well as broad diffuse scattering. The latter is centered on the coherent diffraction peak from the GaAs:MnAs matrix, and extends asymmetrically in the $[001]$ direction (ω - 2θ direction) towards negative values. The intensity contours of Fig. 3 are deformed diagonally, especially around the coherent diffraction peak from the GaAs substrate. The diagonal streaks are an experimental artifact induced by the finite size of the detector slit aperture.

Diffuse scattering measurements in conventional HRXRD can be performed in a quite limited range of wave vectors. Therefore, we carried out measurements under grazing-incidence conditions using synchrotron radiation.^{54,56} We measured the diffuse scattering intensity in the GaAs:MnAs granular layer in the vicinity of different reciprocal lattice points. Figure 4 shows ω - 2θ and ω scans across the (220) reflection recorded in a grazing-incidence/grazing-exit geometry, the incidence and exit angles being equal to 0.3° , and an ω scan across the (111) reflection recorded in a grazing-incidence/nongrazing-exit geometry, the incidence angle being 0.3° and the exit angle 10.2° . Narrow slits limited (in two orthogonal directions) the size of the scattered beam entering the detector. Pronounced diffuse scattering is revealed. In ω scans [Figs. 4(b) and 4(c)], the diffuse scattering extends symmetrically. In the ω - 2θ scan across the (220) reflection [Fig. 4(a)], the diffuse scattering intensity distribution is asymmetric, with a higher intensity at the small-angle side of the coherent diffraction peak.

The distribution of the diffuse scattering along radial directions of the reciprocal space is sensitive to the sign of the deformation.^{36,62} The scattering from vacancy-type defect clusters comprises local Bragg scattering from expanded regions immediately surrounding the clusters, and therefore occurs at wave vectors smaller than the reciprocal lattice vector. Conversely, the scattering from interstitial-type defect clusters occurs mainly at larger wave vectors.³⁴ The asymmetric contribution to the diffuse scattering leads then to a higher intensity at smaller angles for vacancy-type defects and a higher intensity at larger angles for interstitial-type defects.^{34,45} The observed asymmetry of the diffuse scattering in our GaAs:MnAs granular layer along radial directions of the reciprocal space [Figs. 3 and 4(a)] indicates that the defect clusters are of vacancy type.

Figure 5 shows a log-log plot of the symmetric part of the diffuse scattering intensity⁶⁴ measured around the (220) and (111) reflections in the granular layer. The three curves of Fig. 4 coincide when they are plotted as a function of $q = |q|$, where $q = Q - G$ is defined as the deviation of the scattering vector Q from the reciprocal lattice vector G . The peak showing up at $q \approx 0.25 \text{ \AA}^{-1}$, in the curve corresponding to the ω - 2θ scan across the GaAs (220) reflection (Fig. 5), is due to coherent diffraction in the MnAs crystallites, as discussed above. Three regions are distinguished in the scat-

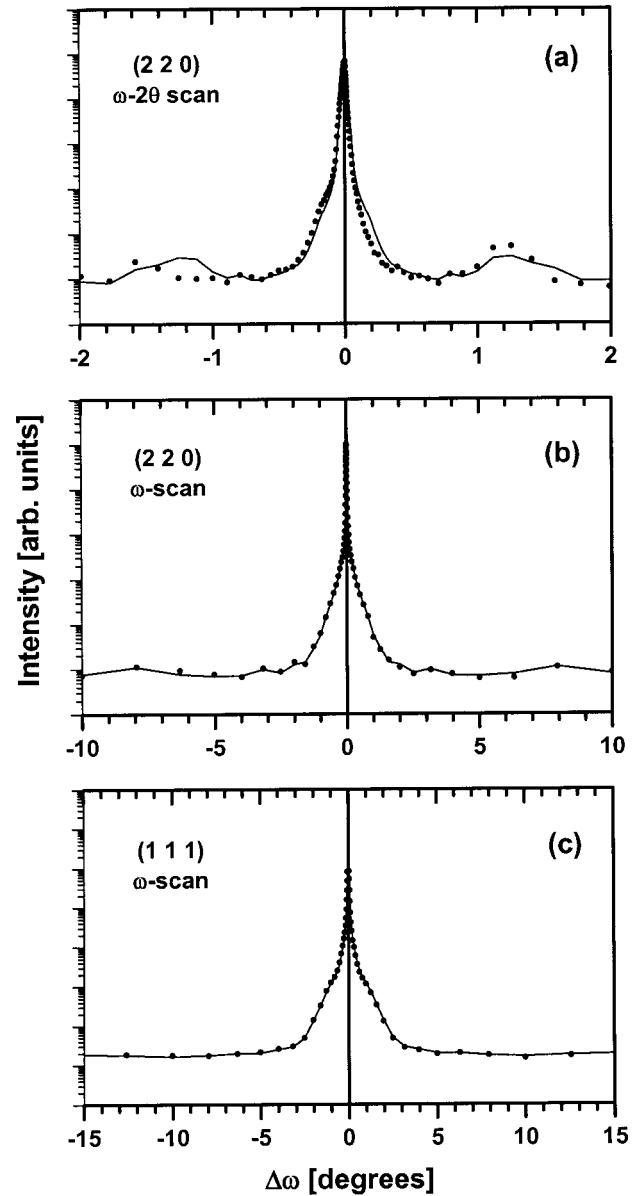


FIG. 4. Grazing-incidence measurements. (a) ω - 2θ and (b) ω scans across the (220) reflection in the matrix of the GaAs:MnAs granular layer for incidence and exit angles equal to the critical angle (0.3°). (c) ω scan across the (111) reflection for an incidence angle of 0.3° and an exit angle of 10.2° . The solid symbols correspond to the raw data, and the solid lines to the symmetric part of the curves.

tered intensity shown in Fig. 5. Their origin can be identified considering the theory of diffuse scattering from crystals with defects.³³⁻⁴² At relatively small wave vectors, the diffuse scattering is due to the far field of elastic distortions around defects. In this region, called Huang diffuse scattering, the symmetric part of the intensity distribution follows an universal law $I_H \sim q^{-2}$. The diffuse scattering at larger wave vectors originates in the vicinity of the defects where the distortions are strong.³⁵ In this region, called asymptotic or Stokes-Wilson scattering, the intensity distribution follows another universal law $I_{SW} \sim q^{-4}$. The intensity of the Stokes-Wilson scattering quickly decreases when the wave vector q

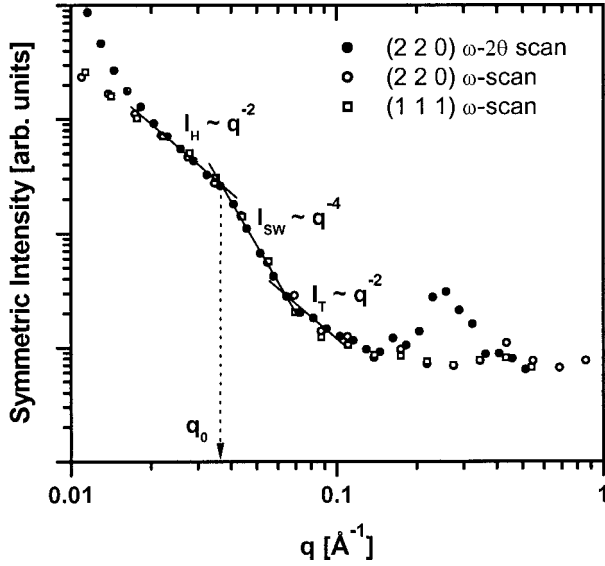


FIG. 5. Log-log plot of the symmetric part of the diffuse scattering close to the (220) and (111) reflections in the GaAs:MnAs matrix. Solid circles correspond to the ω - 2θ scan across the (220) reflection of Fig. 4(a), open circles correspond to the ω scan across the (220) reflection of Fig. 4(b), and open squares correspond to the ω scan across the (111) reflection of Fig. 4(c). The solid lines indicate the exact -2 , -4 , and -2 slopes, which fit the experimental data in the ranges of wave vectors corresponding to the dominant Huang, Stokes-Wilson, and thermal diffuse scattering, respectively. The transition from the Huang to the Stokes-Wilson scattering takes place at the wave vector $q_0 \approx 0.0374 \text{ \AA}^{-1}$.

increases. At sufficiently large q , the scattering from defects becomes weaker than the thermal diffuse scattering, which follows the law $I_T \sim q^{-2}$ (Ref. 65). Thermal diffuse scattering is also present (and described by the same law) at smaller wave vectors, but it cannot be distinguished because of the dominating diffuse scattering from the defect clusters.

An average defect cluster size can be estimated from the value q_0 where the q^{-2} dependence of the Huang diffuse scattering changes to the q^{-4} dependence of the Stokes-Wilson scattering (Fig. 5). This effect has been used⁴⁹⁻⁵³ for experimental estimations of defect cluster sizes. For spherical loose clusters of point defects in an elastically isotropic crystal, for which radial displacement fields simply superimpose on each other,^{33,34} one has

$$q_0 \approx \frac{1}{R_0}, \quad (2)$$

where R_0 is the effective mean radius of the defect clusters. Hence, from the value $q_0 \approx 0.0374 \text{ \AA}^{-1}$ obtained from Fig. 5, the mean diameter of the defect clusters responsible for the diffuse scattering in our GaAs:MnAs layer is estimated to be $d = 2R_0 \approx 5 \text{ nm}$.

The intensity of the Huang diffuse scattering is proportional to the number of defect clusters and, when properly normalized, can be used to determine the cluster density. The intensity of the thermal diffuse scattering provides an internal reference, which can be used to scale the Huang

intensity.⁶⁰ In the Huang region, the symmetric part of the scattered intensity can be expressed as^{36,42}

$$I_H(q) = N_d |f|^2 \frac{(\Delta V)^2}{v^2} \frac{Q^2}{q^2} \Pi(\mathbf{m}, \mathbf{n}), \quad (3)$$

where N_d is the total number of defect clusters in the illuminated sample volume, f is the structure factor, ΔV is the change in the volume of the crystal produced by a single defect cluster, v is the unit cell volume, and $\Pi(\mathbf{m}, \mathbf{n})$ is a dimensionless factor of order 1, which depends on the unit vectors $\mathbf{m} = \mathbf{Q}/Q$ and $\mathbf{n} = \mathbf{q}/q$ and on the elastic constants of the matrix. The Huang intensity in Eq. (3) is expressed in electron units (i.e., with respect to the Thompson scattering from a free electron). The thermal diffuse scattering intensity can be expressed, in the same units, as⁶⁵

$$I_T(q) = |f|^2 \frac{V k_B T/E}{v^2} \frac{Q^2}{q^2} \tilde{K}(\mathbf{m}, \mathbf{n}), \quad (4)$$

where k_B is the Boltzmann constant, T is the temperature of the sample, V is the irradiated volume, E is the Young modulus, and $\tilde{K}(\mathbf{m}, \mathbf{n})$ is another dimensionless factor of order 1. We have introduced the factor $\tilde{K} = EK$, instead of the commonly used factor $K(\mathbf{m}, \mathbf{n})$ (Ref. 65), in order to express the thermal diffuse scattering intensity in analogous form as the Huang scattering intensity. Dividing Eq. (3) by Eq. (4) we obtain

$$\frac{I_H(q_H) |q_H|^2}{I_T(q_T) |q_T|^2} = n_d \frac{(\Delta V)^2}{k_B T/E} \alpha(\mathbf{m}, \mathbf{n}), \quad (5)$$

where $n_d = N_d/V$ is the defect cluster density, q_H is the wave vector in any point of the Huang scattering region, and $I_H(q_H)$ is the measured intensity in that point, while q_T and $I_T(q_T)$ are analogous values in the thermal diffuse scattering region. The dimensionless factor $\alpha = \Pi/\tilde{K}$ is of order 1. For example, for an $[hh0]$ reflection in a cubic crystal and scattering direction along $[110]$, we obtain

$$\alpha = \frac{2(c_{11} + 2c_{12})^2}{9E(c_{11} + c_{12} + 2c_{44})}, \quad (6)$$

using the expressions for Π and K derived in Refs. 36 and 65. Here, c_{11} , c_{12} , and c_{44} are the elastic constants of the matrix. We note that the ratio $k_B T/E$ is a volume that is small compared to the atomic volume. For GaAs at room temperature, $E = 8.53 \times 10^{11} \text{ erg/cm}^3$ (Ref. 66), so that $k_B T/E = 4.8 \times 10^{-5} \text{ nm}^3$. Considering the elastic constants of GaAs,⁶⁶ we obtain $\alpha \approx 0.46$.

The volume change ΔV (the misfit volume) can be obtained from the wave vector q_0 by using the relation⁴²

$$q_0 \approx (GC)^{-1/2}. \quad (7)$$

Here C is the elastic strength of the defect cluster, which determines the displacement field around it: $u(r) = C/r^2$, where r is the distance to the cluster. The crystal is assumed to be elastically isotropic, so that the displacements are radial. The strength C is related to the misfit volume ΔV as follows:

$$C = \frac{1}{12\pi} \frac{1+\sigma}{1-\sigma} \Delta V, \quad (8)$$

where σ is the Poisson ratio. Taking into account the value of q_0 obtained above, the change in crystal volume due to a single defect cluster in the granular layer is $\Delta V \sim 4 \text{ nm}^3$. Using this ΔV value and the measured intensities of the Huang and thermal diffuse scattering (Fig. 5), we obtain from Eq. (5) the density of defect clusters responsible for the diffuse scattering $n_d = 1.8 \times 10^{16} \text{ cm}^{-3}$. This corresponds to a mean distance between clusters $(n_d)^{-1/3} \sim 40 \text{ nm}$.

IV. DISCUSSION

Two different average cluster sizes are derived from the analysis of the diffuse and coherent scattering, 5 nm and 18 nm, respectively. Although both sizes refer to average values, they are experimentally well defined, and seem to be representative of two types of clusters present in the granular layer. The larger size clearly relates to clusters having ordered MnAs structure, since the measured Bragg angle is close to that of bulk hexagonal MnAs. The smaller size, probed by the diffuse scattering, relates to defect clusters producing a large distortion in the matrix lattice.

Transmission electron microscopy (TEM) analysis have confirmed the presence of two types of clusters, with different characteristic sizes, in the sample investigated here (Fig. 6). Our previous TEM studies¹⁷ of phase-separated (Ga, Mn)As material revealed that three different types of clusters can be formed: (1) large spherical clusters with *hexagonal* MnAs structure, (2) small Mn-rich tetrahedral clusters keeping *zinc blende* structure, and (3) small *disordered* Mn-containing clusters inducing a considerable distortion of the lattice. The TEM analysis of the sample investigated here show that there is a high density of small *disordered* clusters and a much lower number of large *hexagonal* MnAs clusters (Fig. 6). Apart from these two types of clusters, the granular layer exhibits high structural quality, and no extended defects have been detected.

The interface between the hexagonal MnAs crystallites and the host matrix is thought to be relaxed to a high extent, so that these clusters induce only a small distortion of the host matrix. The diffuse scattering in the granular layer investigated here is thought to be produced by the disordered Mn-containing clusters, due to the large local lattice distortion that this type of clusters produce. Thus, in the sample investigated here, diffuse and coherent scattering probe different cluster types. The diffuse scattering is sensitive to the

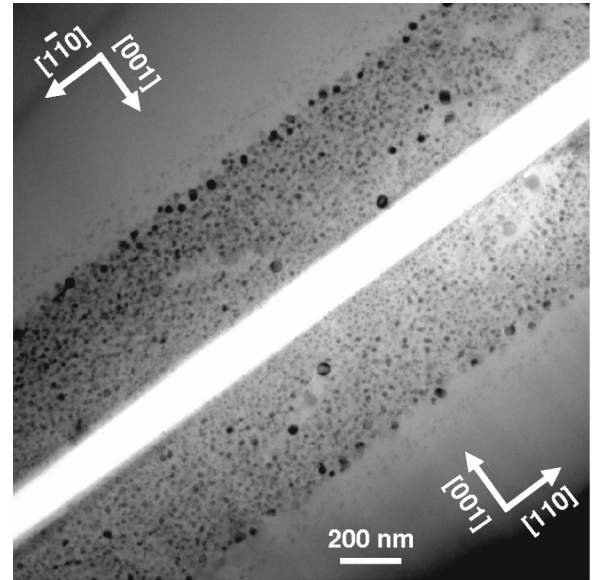


FIG. 6. Cross-sectional bright-field TEM image of two pieces of the annealed (Ga, Mn)As/LT-GaAs/GaAs(001) sample mounted face to face. The bright diagonal line on the micrograph is due to the glue used to prepare the TEM specimen.

small disordered Mn-containing clusters, and coherent scattering probes the larger hexagonal MnAs crystallites. The vacancy-type nature of the small disordered clusters and the higher packing of the hexagonal MnAs crystallite structure compared to the packing of the zinc blende GaAs structure explain the tensile strain developed in the host matrix [Fig. 1(b)].

V. CONCLUSIONS

After thermal annealing of ternary (Ga, Mn)As, two different types of Mn-containing clusters embedded in the GaAs matrix have been detected by x-ray diffuse and coherent scattering. The analysis of the diffuse scattering revealed the existence of small clusters producing a large distortion of the host lattice. Their average size was estimated to be 5 nm, and they were found to be of vacancy-type nature. Coherent diffraction from larger hexagonal MnAs clusters was detected in grazing-incidence measurements, using synchrotron radiation. Their average size was estimated to be 18 nm, and their lattice was found to be compressed along the $[\bar{2}110]$ direction, compared to bulk MnAs. Conventional high-resolution x-ray diffraction measurements revealed that the zinc blende matrix of the granular layer is under tensile strain along directions parallel to the sample surface.

ACKNOWLEDGMENTS

We thank C. Herrmann and H. P. Schönherr for valuable technical assistance. This work was partly supported by the European Commission through the Human Potential Program under Contract No. HP-CT-2000-00134, QMDS, and by the German Federal Ministry of Education and Research (BMBF) under Contract No. 01BM159.

- ¹G.A. Prinz, *Science* **250**, 1092 (1990).
- ²G. Prinz and K. Hathaway, *Phys. Today* (1995), special issue on magnetoelectronics (1995), edited by G. Prinz and K. Hathaway.
- ³G.A. Prinz, *J. Magn. Magn. Mater.* **200**, 57 (1999).
- ⁴H. Ohno, F. Matsukura, and Y. Ohno, *Solid State Commun.* **119**, 281 (2001).
- ⁵D.D. Awschalom, M.E. Flatte, and N. Samarth, *Sci. Am.* **286**(6), 66 (2002).
- ⁶J. De Boeck, W. Van Roy, V. Motsnyi, Z. Liu, K. Dessen, and G. Borghs, *Thin Solid Films* **412**, 3 (2002).
- ⁷J. De Boeck, W. Van Roy, J. Das, V. Motsnyi, Z. Liu, L. Lagae, H. Boeve, K. Dessen, and G. Borghs, *Semicond. Sci. Technol.* **17**, 342 (2002).
- ⁸H. Ohno, *J. Magn. Magn. Mater.* **242**, 105 (2002).
- ⁹R.P. Cowburn, *J. Magn. Magn. Mater.* **242**, 505 (2002).
- ¹⁰J.B. Dai, J.K. Tang, S.T. Hsu, and W. Pan, *J. Nanosci. Nanotechnol.* **2**, 281 (2002).
- ¹¹J. De Boeck, R. Oosterholt, H. Bender, A. Van Esch, C. Bruynseraede, C. Van Hoof, and G. Borghs, *J. Magn. Magn. Mater.* **156**, 148 (1996).
- ¹²J. De Boeck, R. Oosterholt, A. Van Esch, H. Bender, C. Bruynseraede, C. Van Hoof, and G. Borghs, *Appl. Phys. Lett.* **68**, 2744 (1996).
- ¹³H. Akinaga, J. De Boeck, G. Borghs, S. Miyanishi, A. Asamitsu, W. Van Roy, Y. Tomioka, and L.H. Kuo, *Appl. Phys. Lett.* **72**, 3368 (1998).
- ¹⁴H. Akinaga, S. Miyanishi, K. Tanaka, W. Van Roy, and K. Onodera, *Appl. Phys. Lett.* **76**, 97 (2000).
- ¹⁵M. Tanaka, H. Shimizu, and M. Miyamura, *J. Cryst. Growth* **227**, 839 (2001).
- ¹⁶H. Shimizu and M. Tanaka, *J. Appl. Phys.* **89**, 7281 (2001).
- ¹⁷M. Moreno, A. Trampert, B. Jenichen, L. Däweritz, and K.H. Ploog, *J. Appl. Phys.* **92**, 4672 (2002).
- ¹⁸P.J. Wellmann, J.M. Garcia, J.-L. Feng, and P.M. Petroff, *Appl. Phys. Lett.* **71**, 2532 (1997).
- ¹⁹P.J. Wellmann, J.M. Garcia, J.-L. Feng, and P.M. Petroff, *Appl. Phys. Lett.* **73**, 3291 (1998).
- ²⁰S.U. Yuldashev, Y. Shon, Y.H. Kwon, D.J. Fu, D.Y. Kim, H.J. Kim, T.W. Kang, and X. Fan, *J. Appl. Phys.* **90**, 3004 (2001).
- ²¹H. Akinaga, M. Mizuguchi, T. Manago, E. Ganshina, A. Granovsky, I. Rodin, A. Vinogradov, and A. Yurasov, *J. Magn. Magn. Mater.* **242**, 470 (2002).
- ²²J.M. Daughton, *Thin Solid Films* **216**, 162 (1992).
- ²³H. Shimizu, M. Miyamura, and M. Tanaka, *Appl. Phys. Lett.* **78**, 1523 (2001).
- ²⁴B. Jenichen, W. Braun, V.M. Kaganer, A.G. Shtukenberg, L. Däweritz, C.G. Schulz, K.H. Ploog, and A. Erko, *Rev. Sci. Instrum.* **74**, 1267 (2003).
- ²⁵J.W. Du Mond, *Phys. Rev.* **52**, 872 (1937).
- ²⁶W.J. Bartels, *J. Vac. Sci. Technol. B* **1**, 338 (1983).
- ²⁷The Mn content was estimated using Vegard's law, considering for (Ga, Mn)As the same elastic constants as for GaAs, and neglecting the strain induced by As_{Ga} antisites, which are likely to be present.
- ²⁸A. Trampert (unpublished).
- ²⁹R. Feidenhans'l, *Surf. Sci. Rep.* **10**, 105 (1989).
- ³⁰The bulk MnAs interplanar distance along the $[\bar{2}110]$ direction has been calculated considering for the hexagonal MnAs structure the lattice constants: $a = 3.72 \text{ \AA}$ and $c = 5.71 \text{ \AA}$, taken from *Powder Diffraction File*, ICDD, Swarthsmoor, Pennsylvania, No. PDF 280644.
- ³¹P. Scherrer, *Nachr. Göttinger Gesell.* **98**, (1918); Zsigmondy's *Kolloidchemie*, 3rd ed., p. 394.
- ³²B.E. Warren, *X-Ray Diffraction* (Dover, New York, 1990).
- ³³P.H. Dederichs, *Phys. Rev. B* **1**, 1306 (1970).
- ³⁴P.H. Dederichs, *Phys. Rev. B* **4**, 1041 (1971).
- ³⁵H. Trinkaus, *Z. Angew. Phys.* **31**, 229 (1971).
- ³⁶H. Trinkaus, *Phys. Status Solidi B* **51**, 307 (1972).
- ³⁷H. Trinkaus, *Phys. Status Solidi B* **54**, 209 (1972).
- ³⁸P.H. Dederichs, *J. Phys. F: Met. Phys.* **3**, 471 (1973).
- ³⁹P. Ehrhart, H. Trinkaus, and B.C. Larson, *Phys. Rev. B* **25**, 834 (1982).
- ⁴⁰S. Iida, B.C. Larson, and J.Z. Tischler, *J. Mater. Res.* **3**, 267 (1988).
- ⁴¹V. Holy and J. Kubena, *Phys. Status Solidi B* **170**, 9 (1992).
- ⁴²M.A. Krivogla, *X-Ray and Neutron Diffraction in Nonideal Crystals* (Springer-Verlag, Berlin).
- ⁴³H. Peisl, *J. Appl. Crystallogr.* **8**, 143 (1975).
- ⁴⁴P. Ehrhart, *J. Nucl. Mater.* **216**, 170 (1994).
- ⁴⁵J.E. Thomas, T.O. Baldwin, and P.H. Dederichs, *Phys. Rev. B* **3**, 1167 (1971).
- ⁴⁶P. Ehrhart and W. Schilling, *Phys. Rev. B* **8**, 2604 (1973).
- ⁴⁷B.C. Larson and F.W. Young, Jr., *Z. Naturforsch. A* **28A**, 626 (1973).
- ⁴⁸J.R. Patel, *Appl. Crystallogr.* **8**, 186 (1975).
- ⁴⁹K. Lal, B.P. Singh, and A.R. Verma, *Acta Crystallogr., Sect. A: Cryst. Phys., Diffr., Theor. Gen. Crystallogr.* **35**, 286 (1979).
- ⁵⁰W. Mayer and H. Peisl, *J. Nucl. Mater.* **108/109**, 627 (1982).
- ⁵¹A.A. Lomov, P. Zaumseil, and U. Winter, *Acta Crystallogr., Sect. A: Found. Crystallogr.* **41**, 223 (1985).
- ⁵²S. Hahn, F.A. Ponce, W.A. Tiller, V. Stojanoff, D.A.P. Bulla, and J. Castro, *J. Appl. Phys.* **64**, 4454 (1988).
- ⁵³K. Lal and G. Bhagavannarayana, *J. Appl. Crystallogr.* **22**, 209 (1989).
- ⁵⁴S. Grotehans, G. Wallner, E. Burkel, H. Metzger, J. Peisl, and H. Wagner, *Phys. Rev. B* **39**, 8450 (1989).
- ⁵⁵M. Yoon, B.C. Larson, J.Z. Tischler, T.E. Haynes, J.-S. Chung, G.E. Ice, and P. Zschack, *Appl. Phys. Lett.* **75**, 2791 (1999).
- ⁵⁶P. Partyka, Y. Zhong, K. Nordlund, R.S. Averback, I.M. Robinson, and P. Ehrhart, *Phys. Rev. B* **64**, 235207 (2001).
- ⁵⁷K. Karsten and P. Ehrhart, *Phys. Rev. B* **51**, 10 508 (1995).
- ⁵⁸P.O. Renault, A. Declémy, P. Leveque, C. Fayoux, M. Bessiere, S. Lefebvre, C. Corbel, and L. Baroux, *J. Appl. Phys.* **82**, 609 (1997).
- ⁵⁹A.N. Morozov and V.T. Bublik, *J. Cryst. Growth* **97**, 475 (1989).
- ⁶⁰L.A. Charnyi, K.D. Scherbachev, and V.T. Bublik, *Phys. Status Solidi A* **128**, 303 (1991).
- ⁶¹L.A. Charniy, A.N. Morozov, V.T. Bublik, K.D. Scherbachev, I.V. Stepantsova, and V.M. Kaganer, *J. Cryst. Growth* **118**, 163 (1992).

⁶²K.D. Shcherbachev, V.T. Bublik, and O.E. Daricheva, *Crystallogr. Rep.* **40**, 803 (1995).

⁶³A. Pillukat, K. Karsten, and P. Ehrhart, *Phys. Rev. B* **53**, 7823 (1996).

⁶⁴The symmetric part of the diffuse scattering intensity is obtained

as $I_{\text{symmetric}} = [I_{\text{diffuse}}(+q) + I_{\text{diffuse}}(-q)]/2$.

⁶⁵W.A. Wooster, *Diffuse X-Ray Reflections from Crystals* (Dover, New York, 1997).

⁶⁶S. Adachi, *J. Appl. Phys.* **58**, R1 (1985).